Microchimica Acta (2021) 188: 407
https://doi.org/10.1007/s00604-021-05054-y

ORIGINAL PAPER

Dendritic porous silica nanoparticles with high-curvature structures for a dual-mode DNA sensor based on fluorometer and person glucose meter

Yulu Wang[1] · Yuemeng Yang[1] · Tingting Wu[1] · Xueji Zhang[2] · Rongming Wang[3] · Xin Du[1,4] · Li-Ping Xu[1,4]

Received: 7 June 2021 / Accepted: 7 October 2021 / Published online: 4 November 2021
© The Author(s), under exclusive licence to Springer-Verlag GmbH Austria, part of Springer Nature 2021

Abstract

A dual-mode DNA sensor was constructed to detect nucleic acid sensitively and selectively. Based on dendritic porous silica nanoparticles (DPSNs) and hybridization chain reaction (HCR) amplification strategy, the fabricated DNA sensor showed good sensitivity with low detection limits down to 2.18 pM and 4.02 pM by fluorescence (excited at 488 nm and emitted at 508 nm) and personal glucose meter (PGM) assays, respectively. This dual-mode detection of DNA offered superior reliability and accuracy and could meet the requirements of different testing environments, including laboratory confirmation and portable detection. Moreover, the impact of nanoparticles morphology on detection performance was also discussed. Due to the center-radial pores, DPSNs had high curvature morphology, which improved the coverage capacity, footprint, and deflection angle of probes. This work fabricated a dual-mode DNA sensor and revealed the relationship between morphology and detection performance, which brought new insights in novel biosensor development.

Keywords DNA sensor · Dendritic porous silica nanoparticles · Dual-mode detection · High curvature structures · Structure-performance relationship

Introduction

Nucleic acids in biological fluids are important biomarkers and can serve as indicators in disease diagnosing, prognosis, and monitoring of therapies [1–4]. Compared with tissue biopsy, the detection of nucleic acids offers noticed advantages including minimum invasion, less time consumption, and ease in measurement and analysis. Currently, great efforts have been made in the fabrication of DNA sensors [5–7]. However, due to the low abundance of target nucleic acids and the homology among family members, the sensitivity of current DNA sensors cannot meet the clinic application requirements.

To further increase the sensitivity and specificity of DNA sensors, several nucleic acid-based amplification strategies are employed [8–13]. Hybridization chain reaction (HCR), an isothermal and enzyme-free signal amplification strategy, has been developed as a nucleic acid amplification strategy [14, 15]. Upon the presence of each copy of the initiator of DNA hairpin molecules, a cascade hybridization can be triggered, thus allowing for the selective and specific detection of DNA, protein, biological molecules, etc.

✉ Xin Du
duxin@ustb.edu.cn

✉ Li-Ping Xu
xuliping@ustb.edu.cn

1 Beijing Key Laboratory for Bioengineering and Sensing Technology, School of Chemistry and Biological Engineering, University of Science and Technology Beijing, Beijing 100083, People's Republic of China

2 Health Science Center, School of Biomedical Engineering, Shenzhen University, Shenzhen 518060, Guangdong, China

3 Beijing Advanced Innovation Center for Materials Genome Engineering, Beijing Key Laboratory for Magneto-Photoelectrical Composite and Interface Science, School of Mathematics and Physics, University of Science and Technology Beijing, Beijing 100083, China

4 Research Center for Bioengineering and Sensing Technology, University of Science and Technology Beijing, 30 Xueyuan Road, Beijing 100083, People's Republic of China

With the boosting advances in nanotechnology, various nanomaterials with distinct properties like fine nanostructures have been employed to construct DNA sensors to achieve better biosensing performance. Previous studies have indicated that nanostructures are highly beneficial for sensitive bio-detection. Among those nanomaterials, porous silica nanoparticles have attracted great attention due to their excellent biocompatibility, high specific surface area, tunable pore structure, and controllable pore size [16–18]. The dendritic porous silica nanoparticles (DPSNs) with center-radial large channels are finely nanostructured with high curvature surfaces, showing outstanding properties of high pore volume and accessible internal surface. It can be anticipated that DPSNs can provide more active sites and achieve high encapsulation of biomolecules, thus making them promising for biosensing applications [19–21]. Despite the rapid progress in nanomaterial-based biosensors, the relationship between nanomaterial morphology and detection performance was not clarified. The physic origin of nanomaterial enhancement in sensitivity needed to be revealed.

Currently, most biosensors rely on single-mode readout, which may suffer from several interferents and cause false-positive signals. In this work, we fabricated a dual-mode DNA sensor based on DPSNs with high-curvature surfaces. In the presence of the target, the capture probe and reporter probe would hybridize with the target, and then it would trigger HCR reaction by opening the hairpin structure of detection probes, which were labeled with FAM and invertase. Thus, this biosensor could output fluorescence intensity and glucose concentration signal to achieve dual-mode detection of nucleic acid. The large specific surface area of DPSNs improved the surface coverage capacity and footprint of probes. Immobilizing on the accessible internal surfaces of DPSNs, capture probes had low curvature radius and large deflection angle and then promoted detection sensitivity. This work has great potential in nucleic acid identification and disease diagnosis by satisfying the requirements of DNA detection in different situations and provides new insight for biosensor fabrication based on the structure-performance relationship discussed in this work.

Experiment, results, and discussion

Experimental section

Firstly, monodispersed DPSNs were synthesized by using CTA·Tos and [BMIM]OTF as surfactants, TEA as mineralizing agent, TEOS as silica precursor, and water as solvent [22, 23]. Secondly, the functionalization of aminopropyl group (-$(CH_2)_3$-NH_2) on the surface of DPSNs was carried out via the post-grafting method [22]. Thirdly, the conjugation of DPSNs-NH_2 with an amino-modified capture probe was performed by the glutaraldehyde conjugation method. Finally, the H1-invertase conjugates were prepared according to the previous methods with some modifications [5]. More details about the experiment procedures are listed in the supporting information.

Principle of the dual-mode DNA sensor

The principle of this dual-mode DNA sensor is illustrated in Fig. 1. In the presence of target, DPSNs-capture conjugate formed a sandwich structure of "capture-target-reporter" firstly. The exposed sequence of reporter probe further triggered HCR through hybridizing with the sticky end of H2-FAM and opened its hairpin structure by strand exchange reaction. The opened structure of H2-FAM exposed a new region that acted as an initiator sequence and further opened the hairpin structure of H1-invertase. After a few cycles, a double-helix polymer labeled by FAM and invertase, which was called "capture-target-reporter-HCR," was constructed and immobilized on the DPSNs. Fluorescence intensity signal (excited at 488 nm and emitted at 508 nm) was recorded by a fluorescence spectrometer. Meanwhile, the glucose concentration was quantified by a PGM after the invertase converted sucrose into glucose. Thus, based on the above principle, this biosensor could achieve dual-mode detection of DNA.

Characterizations of DPSNs and DPSNs-capture conjugates

The fabricated DPSNs were characterized by SEM and TEM. The SEM and TEM images in Fig. 2A–B reflected that the extracted DPSNs possessed uniform particle size (259.57 ± 16.41 nm) and dendritic-like center-radial pores. The thickness of the pore wall was 17.76 ± 16.41 nm. The nitrogen adsorption–desorption isotherm of DPSNs in Fig. S1A showed a type IV isotherm, and BET-specific surface area of DPSNs was calculated to be 244.43 m^2/g from the adsorption branch of the isotherm. Total pore volume was determined to be 0.60 cm^3/g from the amount of N_2 adsorbed at the single point of $P/P_0 = 0.98$. According to the DFT method, there were several peaks between 1 and 35 nm in Fig. S1B indicating the presence of center-radial mesopores with wide pore size distribution, which provided more active sites for probe immobilization.

The preparation process of DPSNs-capture conjugate was characterized by the zeta potential value as shown in Fig. 2C. The zeta potential value was − 35.5 mV (DPSNs) because the silanol groups on the surface of DPSNs provided negative charges. After aminopropyl functionalization of DPSNs, the zeta potential value changed to + 39.8 mV (DPSNs-NH_2), indicating the successful grafting of the aminopropyl groups on DPSNs. The zeta potential value of

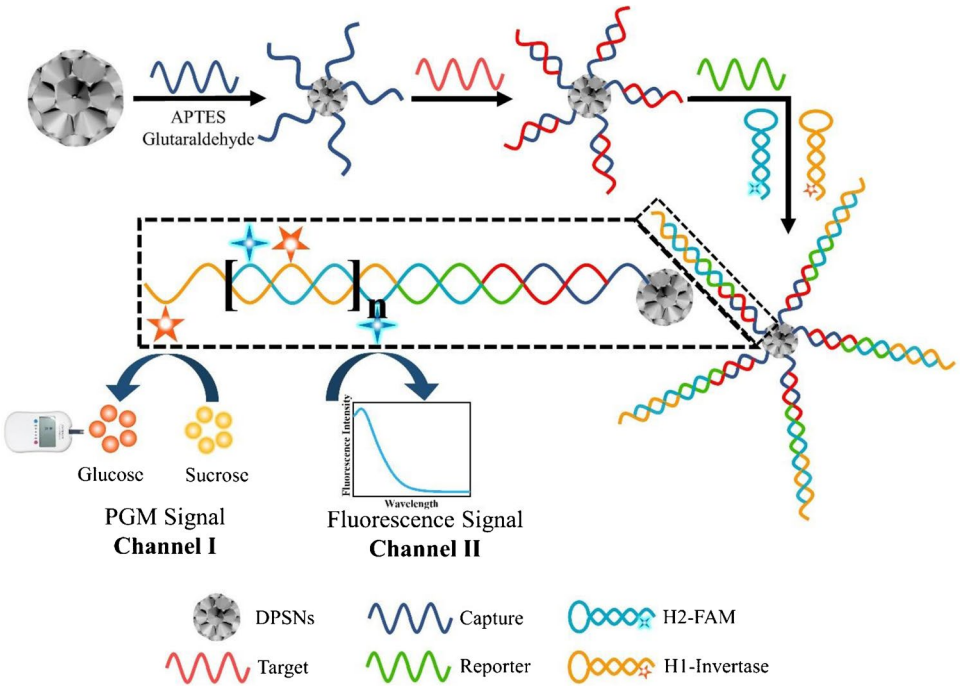

Fig. 1 Schematic illustration of the principle of this dual-mode DNA sensor including the partially enlarged view of the structure of "capture-target-reporter-HCR" on DPSNs

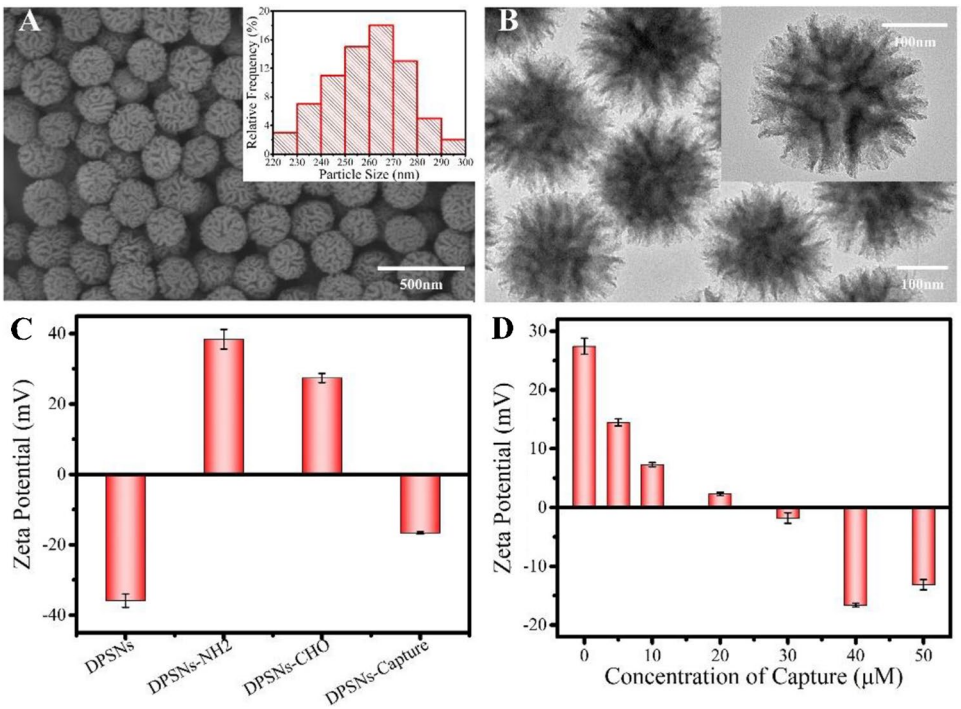

Fig. 2 Characterization of DPSNs and DPSNs-capture conjugates. **A** SEM image of DPSNs (the inset is the corresponding particle size distribution). **B** TEM images of DPSNs. **C** Surface zeta potential value of DPSNs, DPSNs-NH_2, DPSNs-CHO, and DPSNs-capture conjugate in deionized water. **D** Surface zeta potential values of DPSNs-capture conjugates prepared at different concentrations of capture probe in deionized water

DPSNs-CHO (+ 27.4 mV) was lower than that of DPSNs-NH_2 but higher than that of DPSNs-capture (− 16.6 mV). It could be ascribed to the negatively charged phosphate groups of nucleic acids, indicating successful attachment of capture probe. It was worth mentioning that the zeta potential value of DPSNs-capture conjugates (Fig. 2D) declined as the concentration of capture probe increased and reached the lowest point of − 16.6 mV when the concentration was 40 μM. Thus, 40 μM of capture probe was selected as saturation concentration and used in the following experiments.

To confirm the conjugation of DPSNs and capture probe, the UV–Vis absorption spectra of DPSNs, capture probe, and DPSNs-capture conjugate were recorded by a spectrophotometer (Fig. S2). The absorption peak of

DPSNs-capture conjugate (the green line) at 265 nm implied the successful immobilization of capture probe on DPSNs.

Feasibility of the DNA sensor

The feasibility of the proposed DNA sensor was studied by agarose gel (4%) electrophoresis. As shown in Fig. S3, the capture probe in lane 1 escaped from the gel and could not be observed, which might be ascribed to its short oligonucleotide sequence [24]. Lanes 2–3 represent target and reporter probe, respectively. As shown in lane 4, there was a new band at a shorter electrophoresis distance, which could be attributed to the formation of "capture-target-reporter" with higher molecular weight. Lanes 5–8 were reporter probe, H1, H2, and the mixture of H1 and H2, respectively. Compared with lane 8, the mixture of reporter probe, H1, and H2 in lane 9 exhibited multiple trailing bands with molecular weight exceeding 50 bp, suggesting that the HCR reaction was triggered successfully and the complex "reporter-HCR" with a higher molecular weight was generated. The result of gel electrophoresis implied that a cascade hybridization had been triggered successfully by the target.

Analytical characteristics

Under the optimal conditions, the performance of this dual-mode DNA sensor was evaluated at two different modes. Figure 3 A showed the change of fluorescence intensity with the increasing concentration of target. A good linear response between fluorescence intensity and the logarithm concentration of target ranging from 0.1 to 1000 nM was observed. The regression equation was FI = 162.48 lg C + 994.02 with a correlation coefficient R^2 of 0.9809 (FI, fluorescence intensity; C, concentration of target). The detection limit for the fluorescence signal was calculated to be 2.18 pM. Meanwhile, PGM signal, as depicted in Fig. 3B, exhibited the same linear range as fluorescence intensity with the upswing of target concentration. The regression equation was PGM = 3.58 lg C + 16.24 with a correlation coefficient R^2 of 0.9880 (PGM, PGM signal; C, concentration of target). The detection limit for PGM signal was calculated to be 4.02 pM. The detection limits were calculated based on the background signal plus three times the standard deviation of the background signal. Compared with the analytical characteristics of recently reported nanomaterial-based fluorescent sensing for the detection of nucleic acid

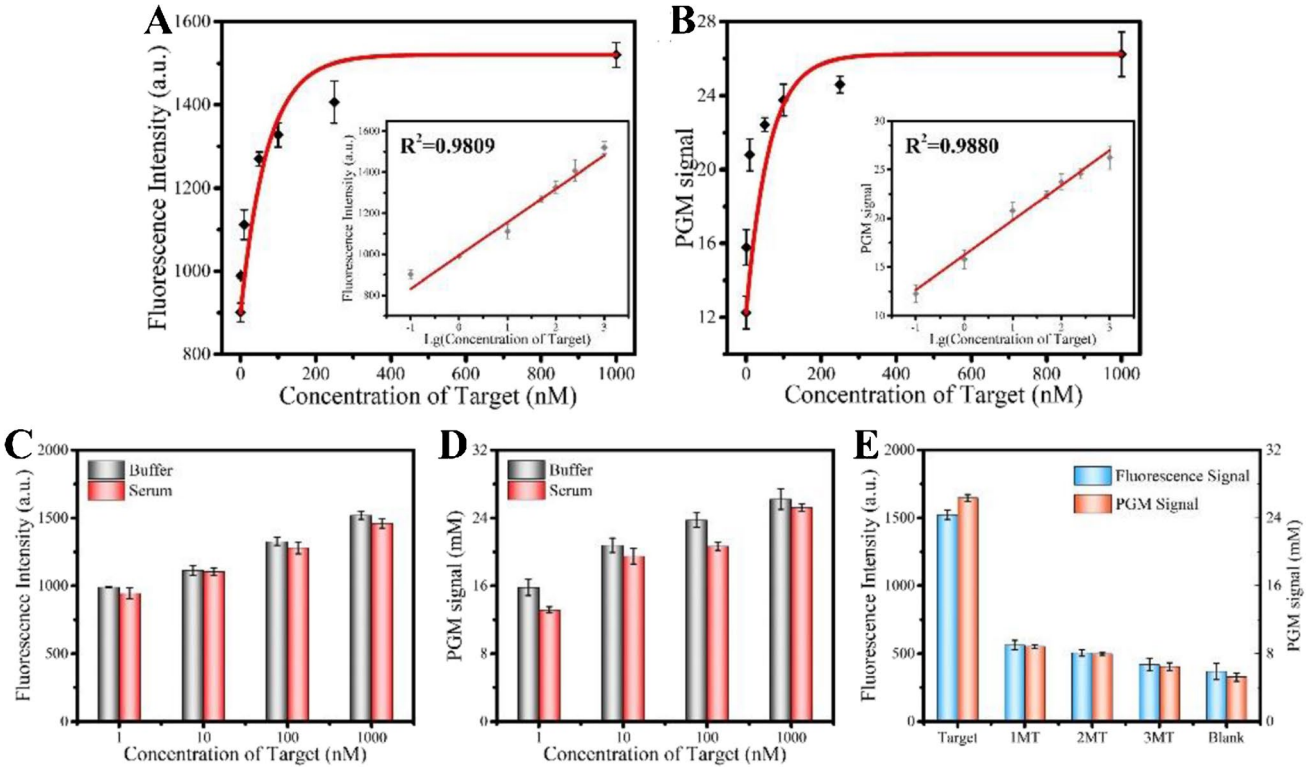

Fig. 3 Performance of the dual-mode DNA sensor. The calibration curve of **A** fluorescence intensity (the excitation wavelength was 488 nm and the emission wavelength was 508 nm) and **B** PGM signal in working buffer versus the logarithm concentrations of the target. **C** and **D** Performance of DNA sensor in serum corresponding to various concentrations of target compared with that in working buffer. **E** Fluorescence intensity (in blue) and PGM signal (in orange) in the presence of the target, 1MT, 2MT, 3MT, and buffer solution. The concentration of targets was 100 nM

(Table S1), this dual-mode biosensor showed good detection performance.

To demonstrate a possible application of the fabricated DNA sensor, the performance of this dual-mode DNA sensor in serum was also evaluated. As shown in Fig. 3C–D, the values of fluorescence and PGM signal in serum were a little lower than those in working buffer. The reason was speculated that the probe in serum was prone to interferences by biomatters which was inevitable in a complex environment like serum, blood, and cells. For the fluorescence assay, the strong fluorescence background induced by biomatters would screen off the light used for fluorescence excitation and emission and thus weaken the signal. However, it is a system error that will not affect the test result. The changing trend of the values of fluorescence and PGM signal in serum was consistent with the results measured in the working buffer. The regression equations in serum were FI = 173.95 lg C + 935.21 with a correlation coefficient R^2 of 0.9992 and PGM = 3.95 lg C + 13.29 with a correlation coefficient R^2 of 0.9843, showing an excellent linear relationship between the detection signals and the logarithm concentration of the target. The comparison of the dual-mode biosensor with the HPLC quantification for target detection in serum is listed in Table S2.

To evaluate the specificity of this biosensor, 1MT, 2MT, and 3MT were also detected with the fabricated sensor. As depicted in Fig. 3E, with the presence of the target, strong fluorescence signal and PGM signal were observed. The fluorescence signal of the target was 4.15 times the signal of blank, and the PGM signal was 5.04 times the signal of blank. While in the presence of the mismatched targets, the same signal values were much lower. The fluorescence signal of 1MT was 0.34 times the signal of target, and the PGM signal was 0.33 times the signal of the target. The fluorescence and PGM signals of 2MT and 3MT were lower and comparable with the background signals. The above results indicated the fabricated biosensor had an admirable selectivity to distinguish the target from other non-complementary nucleic acid sequences.

Effect of surface morphology on detection performance

To confirm the impact of nanoparticle morphology on detection performance, we compared the sensitivity in nucleic acid detection based on two silica nanoparticles with different surface morphologies. Smooth silica nanoparticles (SSNs) with a uniform particle size of 241.16 ± 14.86 nm were synthesized by the previously reported method (Fig. 4A) [25]. The SSNs-capture conjugate was obtained successfully (Fig. 4B), and the SSNs-based dual-mode DNA sensor was fabricated via the same method as the

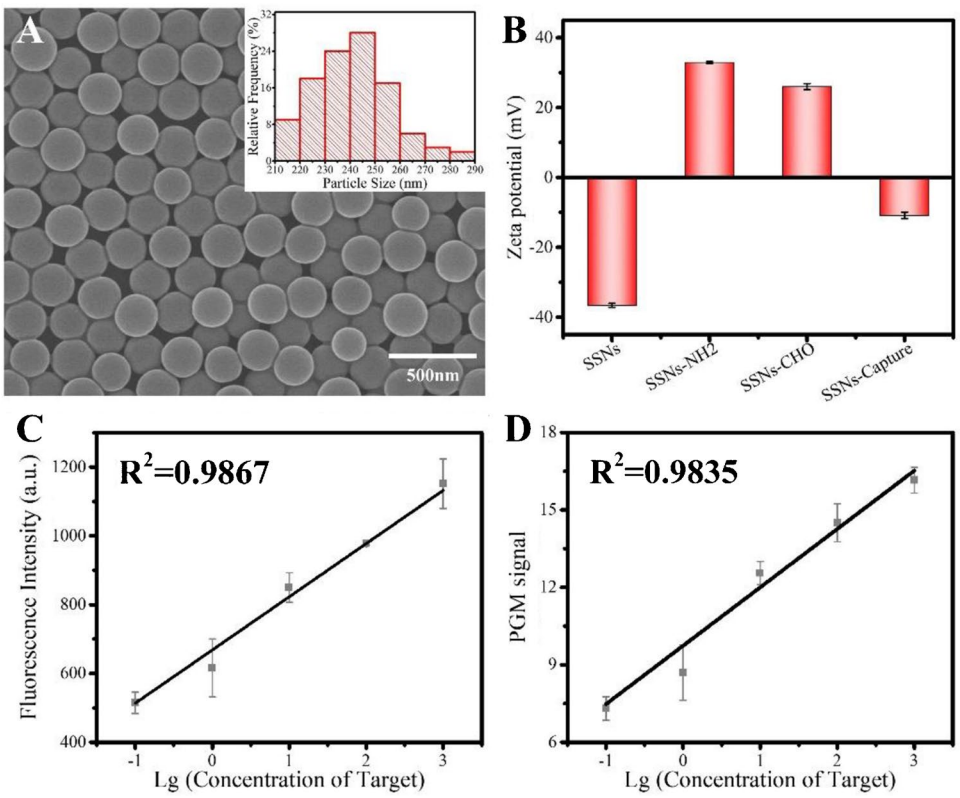

Fig. 4 **A** SEM images of SSNs (the inset is the corresponding particle size distribution). **B** Surface zeta potential value of SSNs, SSNs-NH_2, SSNs-CHO, and SSNs-capture conjugate in deionized water. **C** The calibration curve of the fluorescence intensity and **D** PGM signal of SSNs-based DNA sensor in working buffer versus the logarithm concentrations of the target

DPSNs-based sensor. As shown in Fig. 4C and D, the detection limits of the SSNs-based sensor for fluorescence signal and PGM signal were 204.23 pM and 120.85 pM, respectively.

Firstly, we explored the differences in surface coverage capacity of capture probes on silica nanoparticles with different surface morphologies. FAM-labeled capture probe was employed to conjugate with DPSNs and SSNs. As shown in Fig. 5A, the fluorescence intensity of DPSNs-capture-FAM was higher than that of SSNs-capture-FAM. According to the calibration curve of fluorescence intensity of different concentrations of capture-FAM (Fig. S6), the surface coverage capacity of the capture probe on DPSNs was 2.30×10^{-4} mol/g, which was much higher than that on SSNs (7.16×10^{-5} mol/g). This result indicated that nanoparticles with finely nanostructured surfaces had higher surface coverage capacity than smooth nanoparticles.

Secondly, the hybridization efficiency on different surfaces was evaluated. Several assumptions were made. DPSNs were modeled as spheres with center-radial channels formed by the accumulation of multiple small particles whose diameter was the same as the wall thickness of DPSNs. Capture probes were assumed to be evenly distributed on the particle surfaces. The probe loading density (mol/m^2) of nanoparticles was calculated by dividing the surface coverage capacity (mol/g) by the specific surface area (m^2/g). According to Eq. 1:

$$\text{probe loading density} = \frac{\text{surface coverage capacity}}{\text{specific surface area}} \quad (1)$$

As listed in Table S3, the probe loading density of DPSNs was 9.41×10^{-7} mol/m^2, which was much lower than that of SSNs (6.33×10^{-6} mol/m^2). The effective probe footprint (m^2/n), which was defined as the average area of each capture probe occupied on the nanoparticle surfaces, was one way to think about the spatial arrangement of nucleic acids on nanoparticle surfaces. According to Eq. 2:

$$\text{probe footprint} = \frac{\text{specific surface area}}{\text{surface coverage Capacity} \times N_A} \quad (2)$$

The probe footprint on DPSNs was 1.77×10^{-18} m^2/n, which was much higher than that on SSNs (2.63×10^{-20}

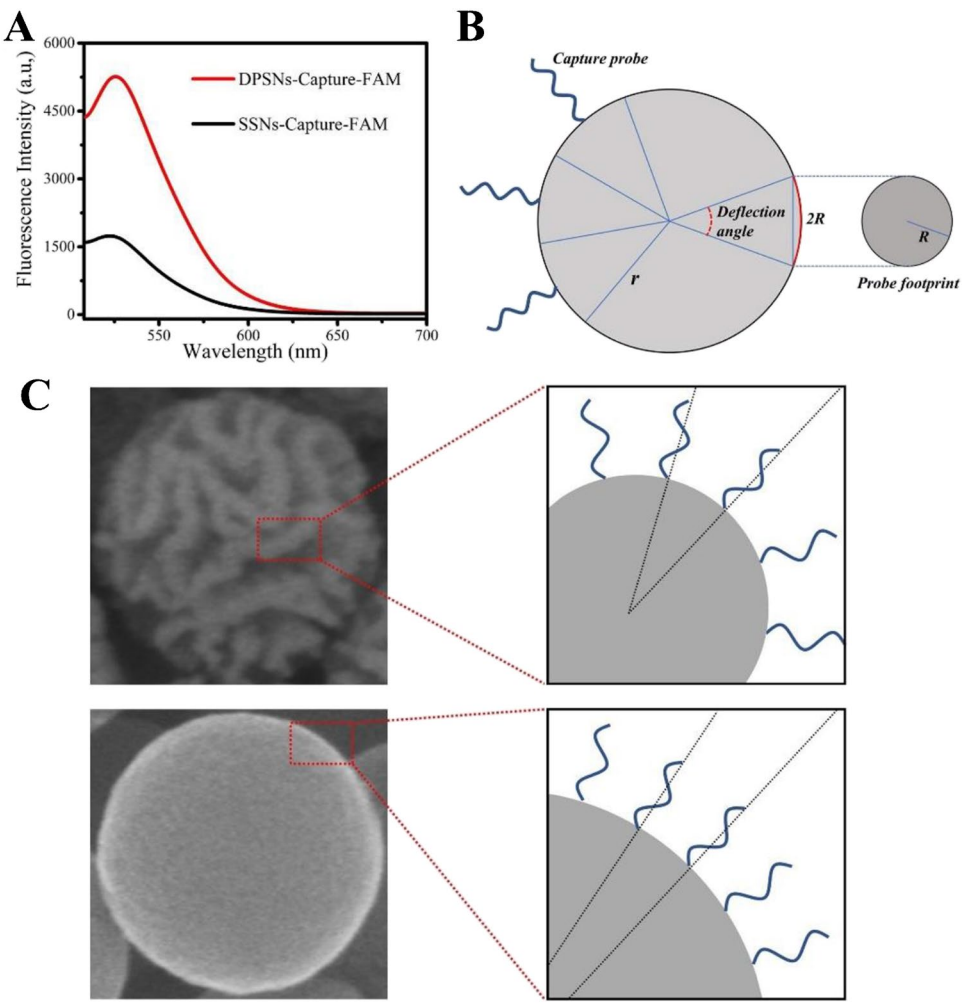

Fig.5 **A** The fluorescence intensity of DPSNs-capture-FAM (in red) and SSNs-capture-FAM (in black). **B** Schematic illustration of the footprint and the deflection angle of the probe. **C** The difference of deflection angle of the probe on DPSNs and SSNs

m^2/n). The average deflection angle (°) between probes attached to the nanoparticle surfaces was directly related to the curvature radius of active sites (r). To calculate the deflection angle between two probes, the capture probe was estimated to be 6 nm in length and adopted a rod-like orientation (rod-like single-stranded DNA, approximately 3 nm/10 bases, was expected to be shorter than fully outstretched 13.4-nm-long single-stranded DNA due to coiling) [26]. According to Eq. 3:

$$2R \times \frac{180}{\text{deflection angle}} = \pi r$$
$$\text{deflection angle} = \frac{360}{\pi^{3/2} r} \times \sqrt{\frac{\text{specific surface area}}{\text{surface coverage capacity} \times N_A}} \quad (3)$$

where R represents the radius of the probe footprint approximation on the nanoparticle surfaces and r is the average curvature radius of active sites (Fig. 5B). The curvature radius of active sites on SSNs (1.21×10^{-7} m) is approximately equal to the radius of particles, while the curvature radius of active sites on DPSNs is not the same as the radius of particles due to the center-radial channels. As shown in Fig. 5C, suppose DPSNs are made up of multiple small particles, whose diameter is the same as the thickness of the pore wall (1.78×10^{-6} nm). The curvature radius of active sites on DPSNs (8.88×10^{-9} m) was approximately equal to half of the pore wall thickness. Thus, the deflection angle of probes on DPSNs was 9.673°, which was much larger than that on SSNs (0.0866°). The improved limits of detection realized with nanoparticles surface morphology stem directly from the large deflection angle.

According to the above discussion, due to the high curvature structures of DPSNs, the higher surface coverage capacity of probes on DPSNs, the larger footprint and deflection angle of probes on DPSNs, and the low steric hindrance for biorecognition accounted for the better hybridization efficiency and detection performance of DPSNs-based DNA sensor [26–30].

Conclusions

In conclusion, a dual-mode DNA sensor based on DPSNs was fabricated. Combining with HCR amplification strategy, the DPSNs-based DNA sensor showed low detection limits down to pM level. Besides, results could be obtained by dual-mode assays, including fluorescence intensity and PGM signal. Due to the high specific surface area and large center-radial pores, DPSNs showed high surface coverage capacity of capture probes, large probe footprint, and deflection angle. Hence, DPSNs had low steric hindrance for biorecognition. This work unraveled the physic origin of nanomaterial enhancement on the detection performance of biosensors and showed great promise in nucleic acid applications.

Supplementary Information The online version contains supplementary material available at https://doi.org/10.1007/s00604-021-05054-y.

Funding This work is supported by the National Natural Science Foundation of China (No. 21890742), National Key R&D Program of China (2019YFA0709300), Fundamental Research Funds for the Central Universities (FRF-TP-19-018B1), and Beijing Municipal Science and Technology Commission (2182036).

Declarations

Conflict of interest The authors declare no competing interests.

References

1. Kaushik AM, Hsieh K, Wang T-H (2018) Droplet microfluidics for high-sensitivity, high-throughput detection and screening of disease biomarkers. Wiley Interdiscip Rev Nanomed Nanobiotechnol 10:1522. https://doi.org/10.1002/wnan
2. Huang R, He N, Li Z (2018) Recent progresses in DNA nanostructure-based biosensors for detection of tumor markers. Biosens Bioelectron 109:27–34. https://doi.org/10.1016/j.bios.2018.02.053
3. Jayanthi VSPKSA, Das AB, Saxena U (2017) Recent advances in biosensor development for the detection of cancer biomarkers. Biosens Bioelectron 91:15–23. https://doi.org/10.1016/j.bios.2016.12.014
4. Xu L-P, Chen Y, Yang G, Shi W, Dai B, Li G, Cao Y, Wen Y, Zhang X, Wang S (2015) Ultratrace DNA detection based on the condensing-enrichment effect of superwettable microchips. Adv Mater 27:6878–6884. https://doi.org/10.1002/adma.201502982
5. Wu T, Yang Y, Cao Y, Song Y, Xu L-P, Zhang X, Wang S (2018) Bioinspired DNA-inorganic hybrid nanoflowers combined with a personal glucose meter for onsite detection of miRNA. ACS Appl Mater Interfaces 10:42050–42057. https://doi.org/10.1021/acsami.8b15917
6. Wu T, Xu T, Xu L-P, Huang Y, Shi W, Wen Y, Zhang X (2016) Superhydrophilic cotton thread with temperature-dependent pattern for sensitive nucleic acid detection. Biosens Bioelectron 86:951–957. https://doi.org/10.1016/j.bios.2016.07.041
7. Zhang X, Wu T, Yang Y, Wen Y, Wang S, Xu L-P (2020) Superwettable electrochemical biosensor based on a dual-DNA walker strategy for sensitive E. coli O157: H7 DNA detection. Sens Actuators B Chem 321:128472. https://doi.org/10.1016/j.snb.2020.128472
8. Wang J, Li T, Li H, Li G, Wu S, Ling L (2019) A universal colorimetric PCR biosensor based upon triplex formation with the aid of Ru(phen)2d ppx2+. Sens Actuators B Chem 278:39–45. https://doi.org/10.1016/j.snb.2018.09.055
9. Tian J, Zhang Y, Zhu L, Tian H, Li K, Huang K, Luo Y, Zhang X, Xu W (2020) dsDNA/ssDNA-switchable isothermal colorimetric biosensor based on a universal primer and λ exonuclease. Sens Actuators B Chem 323:128674. https://doi.org/10.1016/j.snb.2020.128674
10. Ali MM, Li F, Zhang Z, Zhang K, Kang D-K, Ankrum JA, Leb XC, Zhao W (2014) Rolling circle amplification: a versatile tool for chemical biology, materials science and medicine. Chem Soc Rev 43:3324–3341. https://doi.org/10.1039/c3cs60439j
11. Asiello PJ, Baeumner AJ (2011) Miniaturized isothermal nucleic acid amplification, a review. Lab Chip 11:1420–1430. https://doi.org/10.1039/c0lc00666a
12. Huang R, He L, Li S, Liu H, Jin L, Chen Z, Zhao Y, Li Z, Deng Y, He N (2020) A simple fluorescence aptasensor for gastric cancer

exosome detection based on branched rolling circle amplification. Nanoscale 12:2445–2451. https://doi.org/10.1039/c9nr08747h
13. Qin Y, Li D, Yuan R, Xiang Y (2019) Netlike hybridization chain reaction assembly of DNA nanostructures enables exceptional signal amplification for sensing trace cytokines. Nanoscale 11:16362–16367. https://doi.org/10.1039/c9nr04988f
14. Bao T, Wen M, Wen W, Zhang X, Wang S (2019) Ultrasensitive electrochemical biosensor of interferon-gamma based on gold nanoclusters-graphene@zeolitic imidazolate framework-8 and layered-branched hybridization chain reaction. Sens Actuators B Chem 296:126606. https://doi.org/10.1016/j.snb.2019.05.083
15. Wang H-B, Zhong Z-T, Zhang T, Zhao Y-D (2020) Development of dual strip biosensors based on hybridization chain reaction and microplate strategies for signal amplification of HBV-DNA detection. Sens Actuators B Chem 310:127829. https://doi.org/10.1016/j.snb.2020.127829
16. Zhang K, Xu L-L, Jiang J-G, Calin N, Lam K-F, Zhang S-J, Wu H-H, Wu G-D, Albela B, l, Bonneviot L, Wu P, (2013) Facile large-scale synthesis of monodisperse mesoporous silica nanospheres with tunable pore structure. J Am Chem Soc 135:2427–2430. https://doi.org/10.1021/ja3116873
17. Yu Y-J, Xing J-L, Pang J-L, Jiang S-H, Lam K-F, Yang T-Q, Xue Q-S, Zhang K, Wu P (2014) Facile synthesis of size controllable dendritic mesoporous silica nanoparticles. ACS Appl Mater Interfaces 6:22655–22665. https://doi.org/10.1021/am506653n
18. Knezevic NZ, Durand JO (2015) Large pore mesoporous silica nanomaterials for application in delivery of biomolecules. Nanoscale 7:2199–2209. https://doi.org/10.1039/c4nr06114d
19. Wang Y, Du X, Liu Z, Shi S, Lv H (2019) Dendritic fibrous nanoparticles (DFNPs): rising stars of mesoporous materials. J Mater Chem A 7:5111–5152. https://doi.org/10.1039/c8ta09815h
20. Du X, Qiao SZ (2015) Dendritic silica particles with center-radial pore channels: promising platforms for catalysis and biomedical applications. Small 11:392–413. https://doi.org/10.1002/smll.201401201
21. Maity A, Polshettiwar V (2017) Dendritic fibrous nanosilica for catalysis, energy harvesting, carbon dioxide mitigation, drug delivery, and sensing. Chem Sus Chem 10:3866–3913. https://doi.org/10.1002/cssc.201701076
22. Wang Y, Wang Y, Li X, Li J, Su L, Zhang X, Du X (2018) Dendritic silica particles with well-dispersed ag nanoparticles for robust antireflective and antibacterial nanocoatings on polymeric glass. ACS Sustain Chem Eng 6:14071–14081. https://doi.org/10.1021/acssuschemeng.8b02617
23. Lv H, Xing Y, Wang Y, Li X, Zhang X, Du X (2020) Exploration of accessibility of internal pore surface by using rigid nanoparticles as a probe for constructing the integrated nanocomposites. J Alloys Compd 815:152641. https://doi.org/10.1016/j.jallcom.2019.152641
24. Wei J, Chang W, Qileng A, Liu W, Zhang Y, Rong S, Lei H, Liu Y (2018) Dual-modal split-type immunosensor for sensitive detection of microcystin-LR: enzyme-induced photoelectrochemistry and colorimetry. Anal Chem 90:9606–9613. https://doi.org/10.1021/acs.analchem.8b02546
25. Wang Y, Wang Y, Su L, Luan Y, Du X, Zhang X (2019) Effect of surface topology morphologies of silica nanocarriers on the loading of Ag nanoparticles and antibacterial performance. J Alloys Compd 783:136–144. https://doi.org/10.1016/j.jallcom.2018.12.284
26. Hill HD, Millstone JE, Banholzer MJ, Mirkin CA (2009) The role radius of curvature plays in thiolated oligonucleotide loading on gold nanoparticles. ACS Nano 3:418–424
27. Bin X, Sargent EH, Kelley SO (2010) Nanostructuring of sensors determines the efficiency of biomolecular capture. Anal Chem 82:5928–5931
28. Sage AT, Besant JD, Lam B, Sargent EH, Kelley SO (2014) Ultrasensitive electrochemical biomolecular detection using nanostructured microelectrodes. Acc Chem Res 47:2417–2425. https://doi.org/10.1021/ar500130m
29. De Luna P, Mahshid SS, Das J, Luan B, Sargent EH, Kelley SO, Zhou R (2017) High-curvature nanostructuring enhances probe display for biomolecular detection. Nano Lett 17:1289–1295. https://doi.org/10.1021/acs.nanolett.6b05153
30. Wang G, Das J, Ahmed S, Nemr CR, Zhang L, Poudineh M, Sargent EH, Kelley SO (2018) Curvature-mediated surface accessibility enables ultrasensitive electrochemical human methyltransferase analysis. ACS Sens 3:1765–1772. https://doi.org/10.1021/acssensors.8b00494

Publisher's note Springer Nature remains neutral with regard to jurisdictional claims in published maps and institutional affiliations.